

Article

Evaluation and Analysis of the Effectiveness of the Main Mitigation Measures against Surface Urban Heat Islands in Different Local Climate Zones through Remote Sensing

David Hidalgo García 

Department of Architectural Graphic Expression, Technical Superior School of Building Engineering, University of Granada, 18071 Granada, Spain; dhidalgo@ugr.es

Abstract: The significant transformation of land use as a consequence of current population growth, together with global warming (atmospheric emissions and extreme weather events), is generating increases in ambient temperatures. This circumstance is affecting people's quality of life, especially those considered more vulnerable or with fewer economic resources. Currently, 30% of the world's population suffers climatic conditions of extreme heat, and forecasts indicate that in the next 20 years, this number will reach 74%. The present study analyzes the effectiveness of the main mitigation strategies for the surface urban heat island (SUHI) effect between the years 2002 and 2022 in the different local climate zones of the city of Granada (Spain). Using Landsat 5 and 8 images, the evolution experienced by the land surface temperature and the surface urban heat island was determined and connected to the following variables: normalized difference vegetation index, vegetal proportion, normalized difference building index, and albedo. Our results indicate that compact and industrial areas have higher temperatures and lower vegetation and albedo in contrast to open areas, which have lower temperatures and higher vegetation and albedo. The mitigation measures analyzed presented similar efficiencies, but a greater minimization of the SUHI was reported when vegetation was increased in open areas as opposed to in closed areas, where the increase in albedo was more effective. Our study will allow the implementation of more efficient measures based on the types of LCZs in cities.

Keywords: surface urban heat island; land surface temperature; heat mitigation and albedo



Citation: Hidalgo García, D. Evaluation and Analysis of the Effectiveness of the Main Mitigation Measures against Surface Urban Heat Islands in Different Local Climate Zones through Remote Sensing. *Sustainability* **2023**, *15*, 10410. <https://doi.org/10.3390/su151310410>

Academic Editors: Dimitra Founda and George Katavoutas

Received: 24 April 2023

Revised: 24 June 2023

Accepted: 26 June 2023

Published: 1 July 2023



Copyright: © 2023 by the author. Licensee MDPI, Basel, Switzerland. This article is an open access article distributed under the terms and conditions of the Creative Commons Attribution (CC BY) license (<https://creativecommons.org/licenses/by/4.0/>).

1. Introduction

The effects of global warming and extreme weather events are causing significant damage and environmental changes that are affecting people's lives. These changes should be considered some of the most important problems facing humanity [1–4], as recent research showed that the corresponding effects are increasingly intense, last longer, occur more frequently [5,6], and are developing over larger areas [7,8]. The fifth report of the Intergovernmental Panel on Climate Change (IPCC) showed that in recent decades, there has been a significant increase in temperatures leading to significant negative effects on the planet and affecting the health and quality of people's lives, mainly those who live in urban areas [9]. Recent estimates from the United Nations Organization (UNO) project that by the year 2050, the urban population will increase by 20%, from 50 to 70% [10]. These data suggest a population increase of 2.5 billion people that will modify the global urban coverage by 1,600,000 km² [11,12].

The transformation and modification of the soil, mainly motivated by the development of new urban areas generated by population growth, is one of the processes that most strongly affects the increase in global temperatures [4,13]. Changes in different land-use and land-cover (LULC) phenomena reduce evapotranspiration [14] due to the increase in surfaces and spaces built with impermeable materials. During the day, these materials store the heat received from solar radiation, and in the evening–night, they release that heat into

the atmosphere [1,15,16], increasing the ambient temperature. The rise in temperatures within cities is affected by the urban heat island (UHI) phenomenon. The intensity of this phenomenon of climate modification is increased by the actions carried out by people [17], which influence a series of problems that minimize people's quality of life [18]. This circumstance has been shown in recent years by numerous studies on UHI that report higher temperature values in urban areas compared to rural areas, which present lower values [19–21]. Thus, a city with 1 million inhabitants can have an average temperature between 1 and 3 °C higher than that in rural areas [22].

Today, it is estimated that 13.2% of the planet's surface, which is home to 30% of the world's population, suffers from extremely hot weather conditions. In the next 20 years, this number is forecast to reach 74% [23], mainly in the countries of Asia and Central and West Africa [24]. Given this climate emergency situation, it is considered necessary to carry out studies to identify and quantify the most effective urban mitigation and resilience measures for minimizing heat and improving the quality of life for people who live in those areas. There are several commonly studied strategies to reduce the effects produced by the UHI and facilitate the cooling of cities [25,26]. These strategies include increasing the reflectivity of urban surfaces and growing the areas set aside for vegetation [27,28]. Regarding the first measure, it was shown that the waterproof pavements commonly used in urban areas have a high correlation with high temperatures and low reflectivity. These pavements absorb more solar radiation due to their usually dark colors and generate an increase in temperatures. The parameter that regulates the reflection of a surface is albedo, the average value of which in urban areas is 0.30. Techniques that can increase the value of albedo are usually studied to minimize temperatures. For example, a study carried out in Iran reported that a decrease in the mean albedo of 0.02 produced a temperature increase of 0.07 °C [28], a study carried out in the Central Perth Metropolitan Area (Australia) denoted that a decrease in the mean albedo values corresponded to an increase in the LST [29], and a study carried out on the Po River Valley (Italy) using Landsat 8 images reported that an increase in the albedo medium yielded a decrease of 0.5 °C in the SUHI [30]. Finally, a study carried out in the city of Termi (Italy) between the years 2005 and 2015 reported that a decrease of 0.03 in the average albedo increased the surface urban heat island (SUHI) by 2.3 °C [27]. On the other hand, increasing the areas reserved for green spaces and regularly distributing trees in streets and open spaces in cities are considered other effective strategies to prevent environmental warming [31] and minimize pollution. In terms of the intensity of the UHI, the shadows generated by trees prevent solar radiation from heating impermeable and low-albedo walls. Subsequently, due to high levels of thermal absorption, trees release this heat into the atmosphere [20]. On the other hand, the evapotranspiration of plant elements allows plants to shed part of their moisture into the atmosphere, which produces an environmental cooling effect and a decrease in LST [25,32]. In this way, these spaces allow temperatures to be lowered and the effects of the UHI to be minimized, thereby improving the quality of life of the inhabitants. For example, a study on the city of Mumbai (India), in 2018, reported that the green areas of the city presented differences, with urban areas between 2 and 3 K [33]; a study on Singapore between 2005 and 2015 indicated a cooling effect of green areas of between 1 and 3 K [34]; and an investigation in the city of Shenzhen (China) covering 2011 and 2013 observed a drop in temperature between 0.9 and 1.6 K. Although it is common to find studies that analyze certain temperature minimization techniques, few studies analyze the combined effects of both measures on the same urban space in order to assess their possible applications.

Since the 1990s, remote sensing has become one of the most commonly used methods to determine LST, SUHI, and LULC [35]. To understand LST variations, it is essential to study the relationship between those variations and LULC in order to determine how changes in albedo and coverage influence temperature [36]. In studies that consider the morphological conditions of cities [37,38], the use of world-renowned classification is usually common for local climatic zones (LCZs) [39]. LCZs are urban areas or spaces

with the same construction and climatic characteristics that are repeated in all cities, thus allowing one to extrapolate the obtained results.

In this research work, we study the evolution experienced by the variables of albedo, LST, SUHI, and LULC between 2002 and 2022 in the city of Granada (Spain) and the relationship between that evolution and the variables of normalized difference vegetation index (NDVI), normalized difference construction index (NDBI), and vegetation proportion (PV) in order to analyze which commonly used heat mitigation methods may be most suitable for implementation in future urban developments. Among the different existing proposals in the scientific community, the following were chosen: (1) an increase in vegetation, (2) increased albedo, and (3) a combination of proposals 1 and 2. For this analysis, and breaking with the traditional methods of statistical analysis, panel data and ANOVA techniques were used to determine the correlations between the data obtained and the relationship between the variables. This statistical analysis methodology is considered a novel element compared to the traditional multiple correlation methods usually used in research since it allows the incorporation of a greater number of variables and data by admitting the inclusion of individual effects of a certain area and using specific dates to obtain the global results. Therefore, by using this methodology, it is possible to obtain more precise and complex results than those obtained using traditional methods. The location of the area under study near the Mediterranean Sea basin, which was described by some authors as highly vulnerable to climate change [40,41] due to its greater warming compared to other areas of the planet, makes it an appropriate location for this type of study.

The questions that we sought to answer with this research were as follows: (1) What were the spatiotemporal variability and relationships between the albedo, LST, and SUHI variables present in the different LCZs and LULC of the city between the years 2002 and 2022? (2) What relationships exist between the different indices in the different LCZs? (3) How effective would an increase in vegetation and/or albedo be as a SUHI heat mitigation measure? (4) Could the results obtained be important for future urban planning? How could the results obtained affect the development of future urban areas?

This research uniquely provides a complete study on the spatiotemporal variability of the albedo and its relationship with the SUHI and LST on the different LCZs and LULC in the city of Granada and the effectiveness of the mitigation measures commonly used. The overall aim of this research is to promote a considerable improvement in the future and appropriate decision-making by urban planners and public administrations on the development of new urban areas that minimize the effects of heat by SUHI. The development of heat-resilient LCZs will allow urban areas to become resilient to climate change and improve people's quality of life.

2. Materials and Methods

2.1. Area of Study and Data Sources

The area under study is the metropolitan area of the city of Granada (Andalusia), located in southern Spain (Figure 1).

The study area is composed of the city of Granada and 31 more municipalities: Albolote, Alfacar, Alhendin, Armilla, Atarfe, Cajar, Cenes de la Vega, Cijuela, Cullar-Vega, Chauchina, Churriana de la Vega, Dilar, Fuente Vaqueros, Gojar, Guevejar, Hueter-Vega, Jun, Lachar, Maracena, Monachil, Ogijares, Otura, Peligros, Pinos-Genil, Pinos Puente, Pulianas, Santa Fe, Viznar, La Zubia, Las Gabias, and Vegas del Genil. The UTM coordinates are latitude 37.20236 N and longitude 03.29123 W, with an average altitude of 680 m above sea level. The study area (37,790 ha) includes the city of Granada with a population of 278,980 inhabitants and 30 small and medium-sized municipalities (150,000 inhabitants). Thus, the study area encompasses a total population of 428,980 inhabitants and is one of the areas in Andalusia that showed the highest growth in the last decade, together with the areas of Seville and Malaga. This area is located at the foot of the Sierra Nevada mountains, with an average altitude of 2054 m. The Mulhacen peak is located in this mountain range, which, at 3482 m above sea level, is the highest mountain range in all of Western Europe

after the peaks located in the Alps. This area's climate can be classified as transitional between a cold semi-arid climate (Bsk) and Mediterranean climate (Csa), which corresponds to dry and hot summers and mild and humid winters [42]. Average temperatures range from 31 °C in summer to 6 °C in winter. The approximate number of hours of sunshine per year is 2917 h, with an average of 7.99 h of sunshine per day.

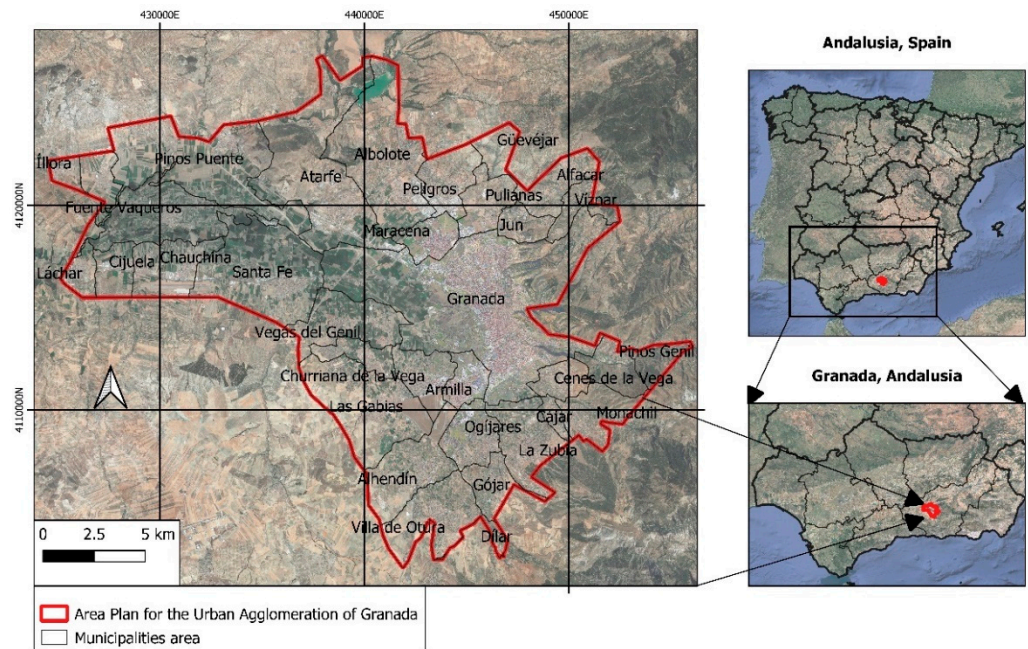


Figure 1. Study area: Granada, Andalusia, Spain.

2.2. Methodology

Figure 2 describes the methodology followed for the development of this research.

Using Landsat 5 and 8 images, the albedo and PV, NDBI, NDVI, and LULC indices of the city were determined at a resolution of 30 and 15 m, respectively. The chosen images correspond to the month of July in 2002, 2012, and 2022. For the classification of land cover, the support vector machine (SVM) methodology was used in the QGIS software, version 3.22.10. The methodology for implementing and obtaining the training data were described in previous investigations [43,44]. On the other hand, determination of the precision of terrestrial cover was carried out by means of a precision matrix. This makes it possible to determine, through cross-validation, the degree of precision obtained in the classification [45]. Next, we identified the five types of LCZ with the greatest development in the study area as follows: compact mid-rise, compact low-rise, industrial, open mid-rise, and open low-rise. These types made it possible to characterize the landscape and urban structure of the city in order to extrapolate the results to other cities that present similar LCZs. The LST and SUHI were obtained through Landsat thermal bands that were subsequently correlated through statistical analysis with the rest of the indices.

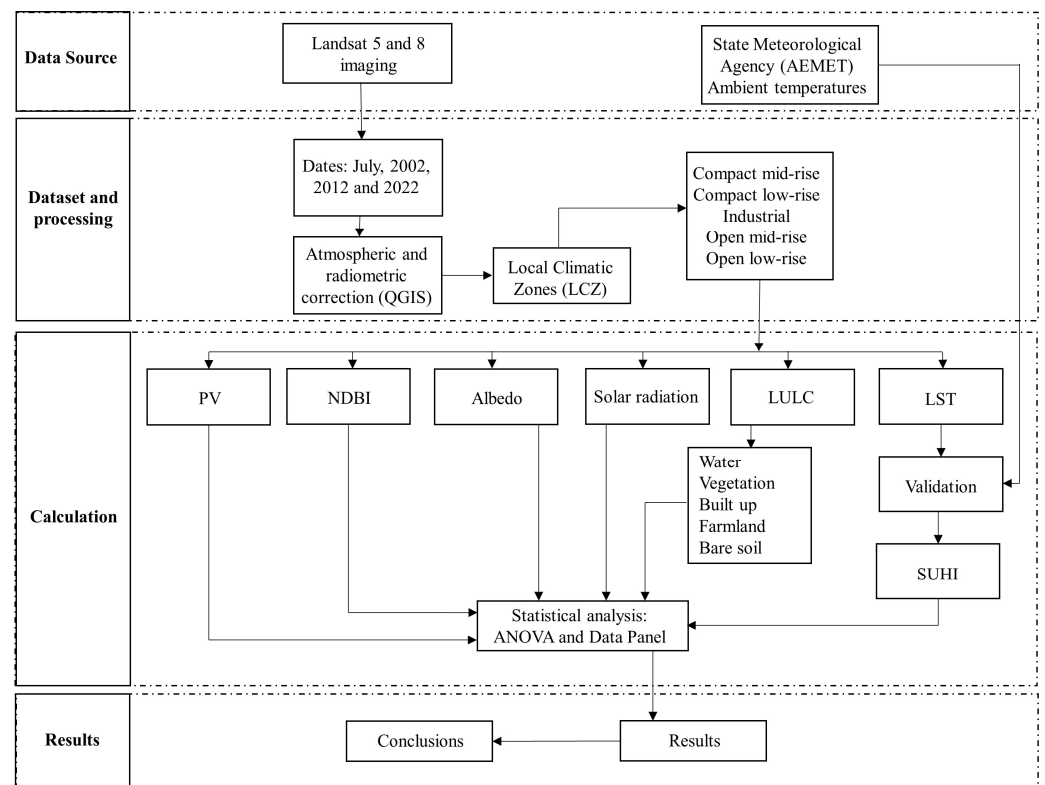


Figure 2. Methodology.

2.3. LCZ Mapping and Classification

Within the metropolitan area of the city of Granada, our research identified the five most developed LCZs: industrial, open (low- and mid-rise), and compact (low- and mid-rise) (Figure 3). These are spaces with similar structures, coverage and human activities that cover a variable area. In this way, each LCZ presents a characteristic regime according to its properties [14] that are maintained over time. Therefore, the identification and cataloging of LCZs may enable the results obtained in this work to be extrapolated to other cities that present the same LCZs. Moreover, the usefulness of LCZs in landscape characterization studies is widely documented [46–49].

Next, a comparative analysis of the different types of coverage obtained by satellite was carried out. For this analysis, 80 reference points were taken. Of these, only four points did not match the satellite images. These values represented 95% coincidence.







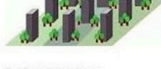


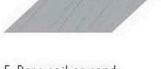
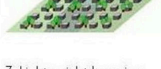






Built types	Definition	Land cover types	Definition
 1. Compact high-rise	Dense mix of tall buildings to tens of stories. Few or no trees. Land cover mostly paved. Concrete, steel, stone, and glass construction materials.	 A. Dense trees	Heavily wooded landscape of deciduous and/or evergreen trees. Land cover mostly pervious (low plants). Zone function is natural forest, tree cultivation, or urban park.
 2. Compact midrise	Dense mix of midrise buildings (3–9 stories). Few or no trees. Land cover mostly paved. Stone, brick, tile, and concrete construction materials.	 B. Scattered trees	Lightly wooded landscape of deciduous and/or evergreen trees. Land cover mostly pervious (low plants). Zone function is natural forest, tree cultivation, or urban park.
 3. Compact low-rise	Dense mix of low-rise buildings (1–3 stories). Few or no trees. Land cover mostly paved. Stone, brick, tile, and concrete construction materials.	 C. Bush, scrub	Open arrangement of bushes, shrubs, and short, woody trees. Land cover mostly pervious (bare soil or sand). Zone function is natural scrubland or agriculture.
 4. Open high-rise	Open arrangement of tall buildings to tens of stories. Abundance of pervious land cover (low plants, scattered trees). Concrete, steel, stone, and glass construction materials.	 D. Low plants	Featureless landscape of grass or herbaceous plants/crops. Few or no trees. Zone function is natural grassland, agriculture, or urban park.
 5. Open midrise	Open arrangement of midrise buildings (3–9 stories). Abundance of pervious land cover (low plants, scattered trees). Concrete, steel, stone, and glass construction materials.	 E. Bare rock or paved	Featureless landscape of rock or paved cover. Few or no trees or plants. Zone function is natural desert (rock) or urban transportation.
 6. Open low-rise	Open arrangement of low-rise buildings (1–3 stories). Abundance of pervious land cover (low plants, scattered trees). Wood, brick, stone, tile, and concrete construction materials.	 F. Bare soil or sand	Featureless landscape of soil or sand cover. Few or no trees or plants. Zone function is natural desert or agriculture.
 7. Lightweight low-rise	Dense mix of single-story buildings. Few or no trees. Land cover mostly hard-packed. Lightweight construction materials (e.g., wood, thatch, corrugated metal).	 G. Water	Large, open water bodies such as seas and lakes, or small bodies such as rivers, reservoirs, and lagoons.
 8. Large low-rise	Open arrangement of large low-rise buildings (1–3 stories). Few or no trees. Land cover mostly paved. Steel, concrete, metal, and stone construction materials.	VARIABLE LAND COVER PROPERTIES Variable or ephemeral land cover properties that change significantly with synoptic weather patterns, agricultural practices, and/or seasonal cycles.	
 9. Sparsely built	Sparse arrangement of small or medium-sized buildings in a natural setting. Abundance of pervious land cover (low plants, scattered trees).	<i>b. bare trees</i>	Leafless deciduous trees (e.g., winter). Increased sky view factor. Reduced albedo.
 10. Heavy industry	Low-rise and midrise industrial structures (towers, tanks, stacks). Few or no trees. Land cover mostly paved or hard-packed. Metal, steel, and concrete construction materials.	<i>s. snow cover</i>	Snow cover >10 cm in depth. Low admittance. High albedo.
		<i>d. dry ground</i>	Parched soil. Low admittance. Large Bowen ratio. Increased albedo.
		<i>w. wet ground</i>	Waterlogged soil. High admittance. Small Bowen ratio. Reduced albedo.

Figure 3. LCZs established by Steward and Oke, 2012 [14].

2.4. Landsat 5 and 8 Images

Landsat images 5 (year 2002 and 2012) and 8 (year 2022) were downloaded via the United States Geological Survey (USGS). The LST was obtained using the thermal bands, while the optical bands were used to calculate the indicated indices. The Landsat 5 Thermal Mapper (TM) data included a total of six multispectral bands (bands 1 to 5 and 7) with a spatial resolution of 30 m and one thermal infrared band (band 6) with a spatial resolution of 120 m. Landsat 8 included a total of 8 multispectral bands (bands 1 to 7 and 9) with a resolution of 30 m and two thermal infrared bands (bands 10 and 11) with a spatial resolution of 100 m. However, to determine the LST with Landsat 8, only band 10 was used. A band resampling process called pansharpening was applied. Therefore, we worked with Landsat bands 5 and 8 at 30 and 15 m resolutions, respectively, using the panchromatic band. The selected images were georeferenced and atmospherically corrected using the dark-object subtraction algorithm (DOS) [50]. This method is commonly employed to atmospherically correct available satellite images, which assumes that the reflectance of dark objects includes a substantial component of atmospheric scattering. In this way, the DOS algorithm searches each band for the darkest pixel value. This algorithm was implemented within the semi-automatic classification plugin (SCP) installed in the QGIS software, version 3.22.10 [51]. This plugin consists of an open source and free access repository that allows the semi-automatic classification of remote sensor images.

2.4.1. Optical Bands

NDVI

The NDVI is calculated using Equation (1) [52]:

$$NDVI = \frac{NIR - Red}{NIR + Red} \quad (1)$$

With the results obtained in Equation (1), the PV can be calculated using Equation (2) [53]:

$$PV = \left[\frac{NDVI - NDVI_{min}}{NDVI_{max} - NDVI_{min}} \right]^2 \quad (2)$$

where NDVI is the index calculated in Equation (1), and NDVI min and max are the minimum and maximum values of the NDVI range, respectively.

LULC

Using the red, green and blue bands of Landsat, the RGB color composition was determined. Next, using the QGIS software, version 3.22.10, the coverage classification method was carried out using a support vector machine (SVM). This methodology is common in soil classification studies that require high precision [43,54].

NDBI

The NDBI shows us the proportion of construction compared to areas without construction in each pixel of a satellite image. The NDBI was calculated using Equation (3) [55]:

$$NDBI = \frac{NIR - SWIR}{NIR + SWIR} \quad (3)$$

Albedo

The broadband total albedo for the study area was retrieved using Equation (4) [27,56], depending on the following coefficients for Landsat bands 5 and 8:

$$Albedo = 0.356 \times B_{Blue} + 0.130 \times B_{Red} + 0.373 \times B_{NIR} + 0.085 \times B_{Swir1} + 0.072 \times B_{Swir2} - 0.0018. \quad (4)$$

2.5. Thermal Bands

2.5.1. Brightness Temperature

First, the brightness temperature (T) in °C was obtained from the spectral radiance through Equation (5) [57]:

$$T = \frac{K_2}{\log\left(\frac{K_1}{L_\lambda} + 1\right)} - 273.15, \quad (5)$$

where K_1 takes values of 607.76 for Landsat 5 and 774.8853 for Landsat 8, and K_2 takes values of 1260.56 for Landsat 5 and 1321.0789 for Landsat 8.

2.5.2. Surface Emissivity (ϵ)

The various surfaces of the earth present different emissivity values depending on their composition, roughness, and structures. The values of brightness temperature (T) estimated using Equation (6) were obtained with the assumption of a general emissivity value equal to 1 (which is a black body). Therefore, spectral emissivity (ϵ) correction should be applied according to the land cover type. The emissivity was calculated according to Equation (6) [58]:

$$\epsilon = 0.004 \times PV + 0.986, \quad (6)$$

where PV is as given by Equation (2).

2.5.3. Land Surface Temperature (LST)

The land surface temperature (LST) was estimated using the land surface emissivity (LSE) values derived from Equation (7) using Equation (8) [59]:

$$LST = \frac{T}{\left(1 + \left(\lambda \frac{T}{C_2}\right) \times \log(\varepsilon)\right)} \quad (7)$$

$$C_2 = \frac{h \times c}{s}, \quad (8)$$

where LST is the temperature of the Earth's surface; T is the brightness temperature of Landsat, $C_2 = 1.4388 \times 10^{-2}$ m K; λ is the wavelength of the emitted radiation (Landsat 5 and 7: $\lambda = 11.457 \mu\text{m}$ and Landsat 8: $\lambda = 10.8 \mu\text{m}$); h is Planck's constant, with a value of 6.626×10^{-34} Js; ε is the emissivity of the ground; c is the speed of light, with a value of 2.998×10^8 m/s; and s is the Boltzmann constant, with a value of 1.38×10^{-23} J/K [59].

2.5.4. SUHI

Using Equation (9), the SUHI can be determined as follows [60]:

$$SUHI = LST_{urban} - LST_{rural}. \quad (9)$$

Urban LST values correspond to the mean values of pixels located within urban areas. The rural LST values used to derive the SUHI were taken in a rural area located about 16 km from the city where a meteorological station of the State Meteorological Agency (AEMET) is located in order to allow subsequent validation of the temperatures.

2.6. Solar Radiation

The solar radiation of the area under study was determined via simulation using the Software System for Automated Geoscientific Analyses (SAGA), version 8.5.1 [61]. This methodology makes it possible to obtain direct, indirect, and total solar radiation based on the digital surface model and its use in studies including solar radiation has been widely validated [62,63].

3. Results

3.1. LCZ Evolution

Figures 4 and 5 show the evolution of the different LCZs investigated in the area under study between 2002 and 2022.

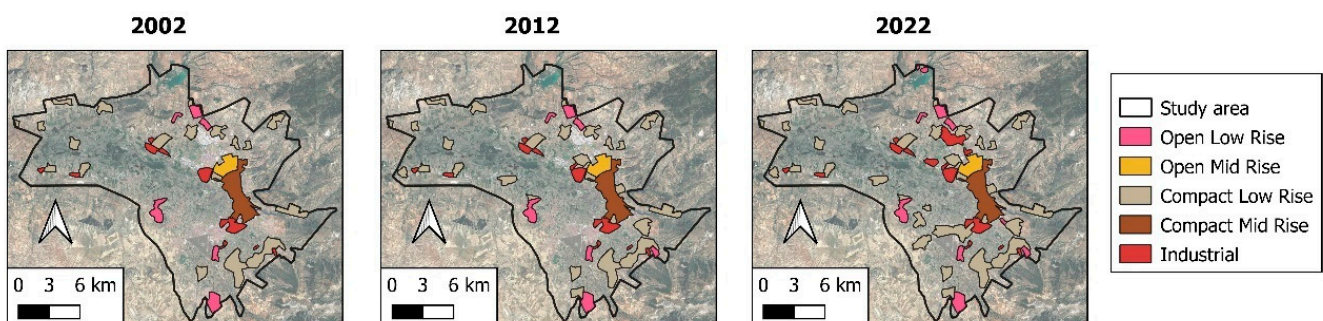


Figure 4. Identification of the LCZs by investigation year.

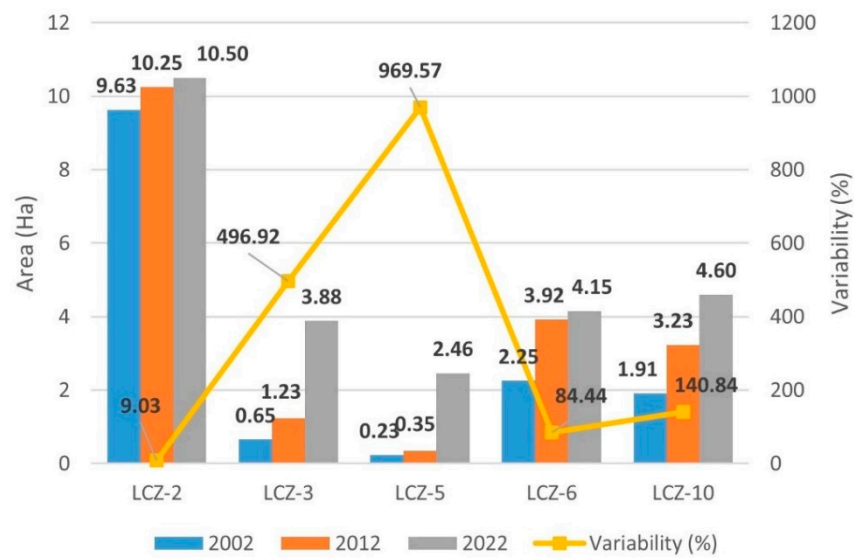


Figure 5. Evolution of the LCZ surface by years investigated.

Here, the greatest surface increases in the different LCZs were observed in the open medium-density zone LCZ-5 (969.57%) and the compact low-density zone LCZ-3 (486.92%). The LCZ-10 industrial zone experienced medium growth (140.84%), while the LCZ-2 medium-density open zone experienced low growth (9.03%).

3.2. Evaluation of the Indices

The spatiotemporal evolution of the indices of the area under study between 2002 and 2022 can be seen in Figures 6–9.

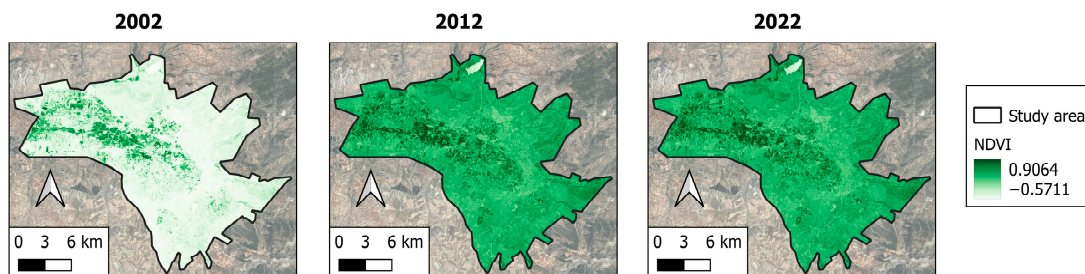


Figure 6. NDVI index between the years 2002 and 2022.

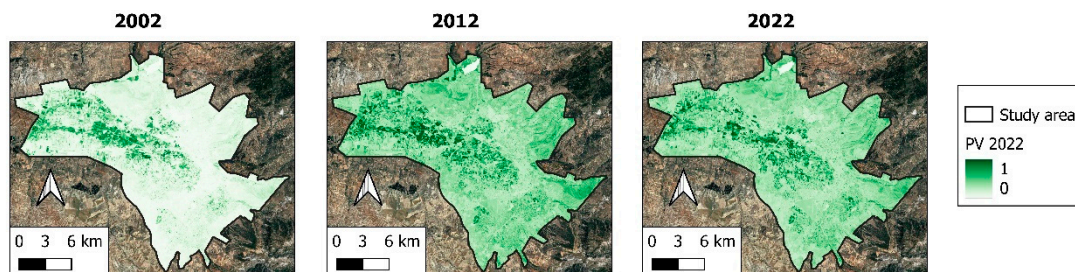


Figure 7. PV index between the years 2002 and 2022.

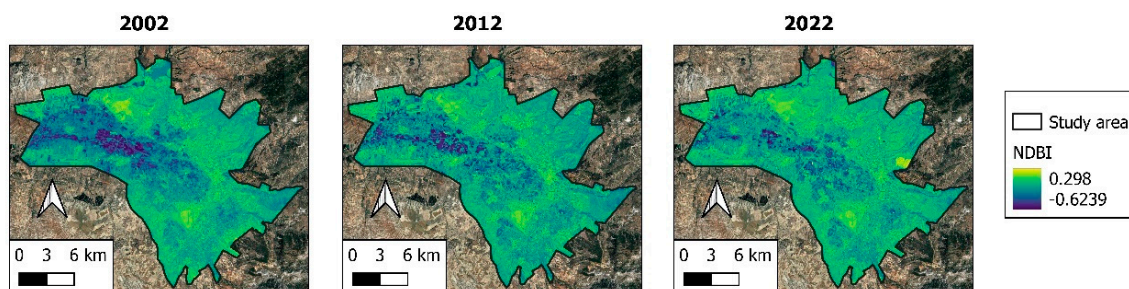


Figure 8. NDBI index between the years 2002 and 2022.

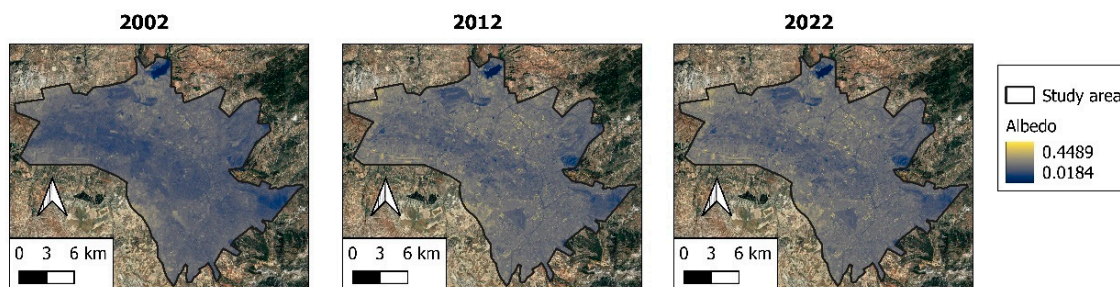


Figure 9. Albedo index between the years 2002 and 2022.

Table 1 shows the mean values of the indices investigated for each LCZ, based on the years investigated.

Table 1. Evolution of the indices studied by LCZ.

Years		LCZ-2	LCZ-3	LCZ-5	LCZ-6	LCZ-10
2002	NDVI	0.126	0.131	0.121	0.204	0.088
	PV	0.043	0.046	0.037	0.111	0.008
	NDBI	0.238	0.139	0.069	0.027	0.005
	Albedo	0.246	0.268	0.241	0.246	0.105
2012	NDVI	0.209	0.215	0.251	0.327	0.115
	PV	0.163	0.182	0.314	0.368	0.010
	NDBI	0.289	0.190	0.090	0.033	0.020
	Albedo	0.187	0.204	0.199	0.210	0.085
2022	NDVI	0.236	0.255	0.255	0.264	0.106
	PV	0.172	0.190	0.316	0.376	0.023
	NDBI	0.359	0.289	0.040	0.123	0.023
	Albedo	0.181	0.198	0.187	0.178	0.074

The first two indices (NDVI) are related to the amount of vegetation that exists in an area and its state of conservation. In contrast, the NDBI is related to buildings and allows for territorial analysis in urban studies. Finally, the albedo reports the reflectivity of the ground with respect to solar radiation. Figure 10 shows the average evolution of the NDVI, PV, NDBI, and albedo values between 2002 and 2012 in the area under study.

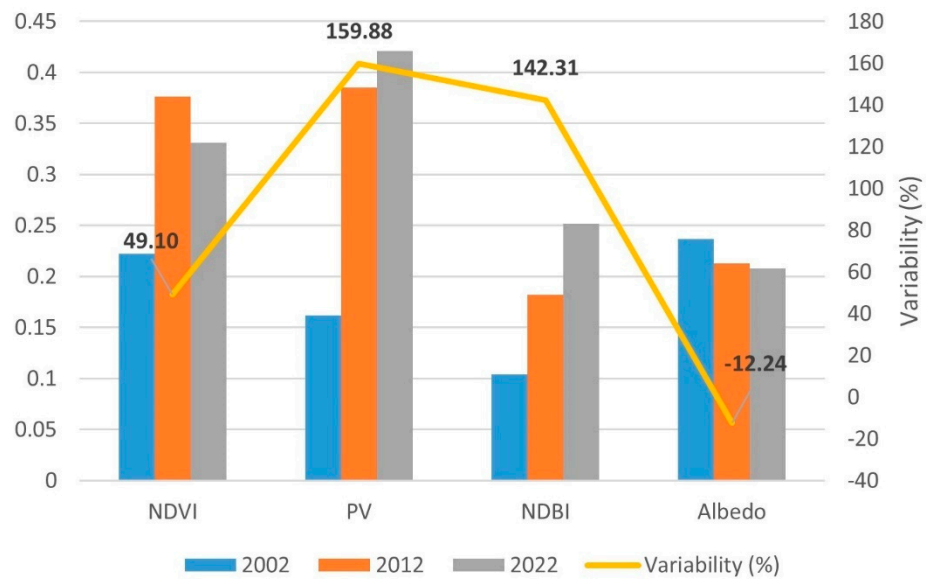


Figure 10. Evolution of the indices between the years 2002 and 2022.

The NDVI obtained a value of 0.222 in the year 2002, 0.376 in the year 2012, and 0.331 in the year 2022, which represents an average increase of 49.10%. The PV obtained a value of 0.162 in 2002, 0.385 in 2012, and 0.421 in 2022, which represents an average increase of 159.88%. The NDBI index obtained a value of 0.104 in 2002, 0.182 in 2012, and 0.252 in 2022, which represents an average increase of 142.31%. Finally, the albedo obtained a value of 0.237 in the year 2002, 0.213 in the year 2012, and 0.208 in the year 2022, which represents an average reduction of 12.34%. In general terms, these values correspond to the standard values for a city with the characteristics of Granada and its metropolitan area. The NDVI and PV values indicate that the vegetation of the studied area can be considered sparse and adequate for the summer period, considering that the selected satellite images correspond to summer. The NDVI values depend not only on the amount of vegetation, which is also important for the PV index, but also on rainfall in the area. Therefore, the reduction of this index in 2022 was related to a decrease in the average rainfall values in the area. Conversely, as the values of PV and NDBI increased, the value of the albedo decreased due to the growth in new urban areas that the city has experienced over time, which minimized vegetation cover and increased the cover of impermeable urban surfaces, minimizing the albedo.

Figure 11 shows the average values of the indices studied in each LCZ. In this way, the NDVI index presents the highest average values in the open areas of LZC-6 (0.265) and LCZ-5 (0.209) and the lowest average values in the closed areas of LZC-2 (0.190) and industrial LCZ-10 (0.103). The PV index also presents the highest mean values in the open areas LCZ-6 (0.285) and LCZ-5 (0.222) and the lowest mean values in the closed areas of LCZ-2 (0.126) and industrial LCZ-10 (0.014). These values indicate that the vegetation is broader and leafier in open areas compared to that in industrial and compact areas of the city.

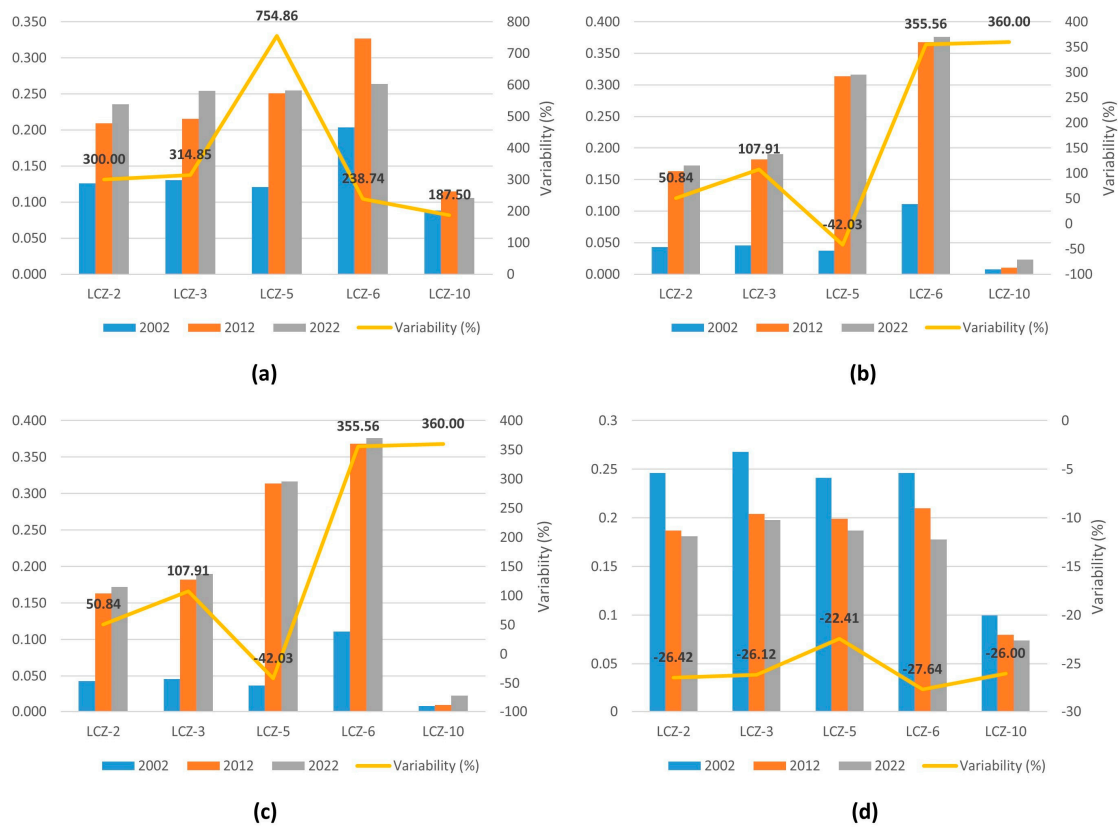


Figure 11. Evolution of the indices (a) NDVI, (b) PV, (c) NDBI and (d) albedo of the area investigated by LCZ.

Here, the NDBI index presents the highest mean values in the compact zones LCZ-2 (0.295) and LCZ-3 (0.206) and the lowest mean values in the open zones LCZ-6 (0.061) and industrial LCZ-10 (0.016). The albedo presents the highest mean values in the open areas LZC-6 (0.211) and LCZ-5 (0.209) and the lowest mean values in the closed areas LCZ-2 (0.205) and industrial LCZ-10 (0.085). These values indicate that buildings have higher occupancy and are denser in compact areas compared to open areas, which translates into lower albedo values in the former compared to the latter.

After applying a Shapiro–Wilk test, the results of the ANOVA test carried out on the NDVI, PV, NDBI, radiation, and albedo indices presented non-normal distributions within the different LCZs since the *p* value was <0.05. Therefore, to continue with the ANOVA analysis for non-normal distributions, it was necessary to perform a Kruskal–Wallis test, the results of which can be found in Table 2.

Table 2. ANOVA test results between the NDVI, PV, NDBI, and albedo indices in the LCZs.

Source	NDVI	PV	NDBI	Albedo	Radiation
<i>p</i> value	0.001 **	0.009 **	0.011 *	0.002 **	0.005 **
R ²	18.25	7.84	7.43	10.59	15.10

Note: errors, ** *p* < 0.01 and * *p* < 0.05. R²: linear regression coefficient.

In these results, the NDVI, PV, solar radiation, and albedo indices present statistically significant relationships of 99% in the different LCZs, while the NDBI variable has a 95% relationship.

3.3. LULC

The space–time evolution of the LULC in the area under study between the years 2002 and 2022 is shown in Figure 12. A reduction in the coverage of water (−10.26%) and

farmland (−7.49%) and an increase in the coverage of vegetation (6.52%), bare soil (7.18%), and built-up land (12.42%) were reported. With respect to the mean values, the coverage with the largest area in 2022 was farmland (48.94%), while the coverage with the smallest area was water (0.57%). Intermediate values were recorded for the coverage of vegetation (14.11%), bare soil (19.68%), and built-up land (16.70%).

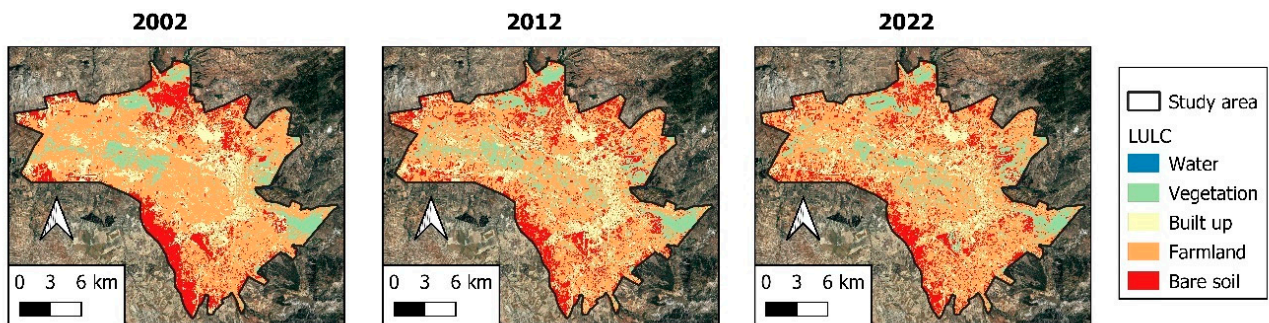


Figure 12. LULC variability of the area under study between the years 2002 and 2022.

Figure 13 shows the different LULC coverage levels by LCZ for the year 2022. The highest built-up coverage was found in LCZ-10 (87.28%), LCZ-2 (43.10%) and LCZ-5 (42.86%). In contrast, the greatest vegetation coverage was found in LZC-6 (4.33%) and LCZ-5 (1.49%). Notably, the compact areas of the city (LCZ-2 and LCZ-3) presented an average built-up coverage (41.41%) greater than that of the open areas (31.77%) (LCZ-5 and LCZ-6). The average vegetation cover was higher in open areas (2.91%) than in compact areas (0.35%). The coverage results obtained were considered adequate for the area under study, taking into account that this area is located in the Mediterranean Sea basin. In turn, these values were in line with the values obtained for the NDVI, PV, and NDBI indices previously obtained. The overall accuracy obtained through the precision matrix was 86.73%, with a 95% confidence interval ranging between 0.73 and 0.91 points.

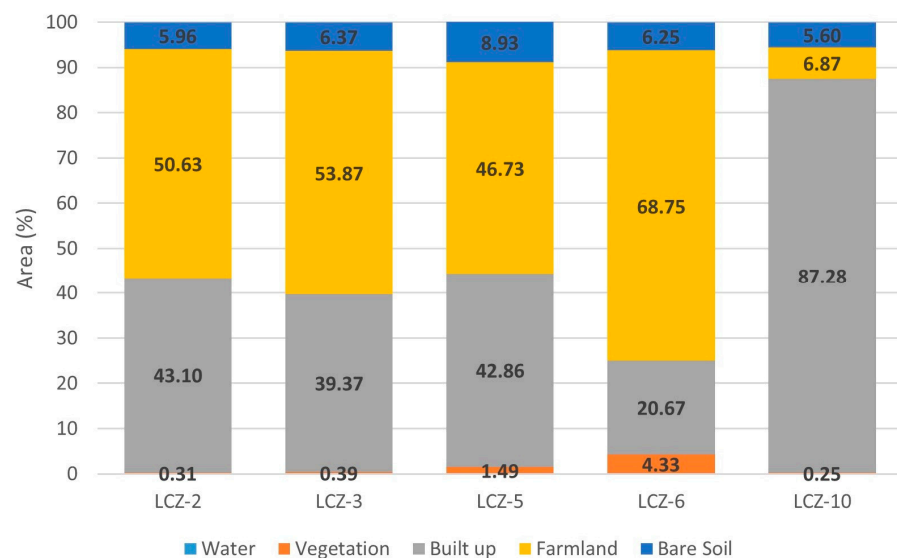


Figure 13. Mean LULC values in the different LCZs.

3.4. LST

Figure 14 shows the space–time evolution of the LST between 2002 and 2022 in the area under study. The average LST in 2002 was 32.66 °C, that in 2012 was 36.48 °C, and that in 2022 was 37.67 °C. These values represent an average increase of 15.34%. It can be seen that the highest values of LST were concentrated in urban areas (with higher values

for the NDBI indices), while the lowest values were located in rural areas or outside the city (with higher values for the NDVI, PV, and albedo indices).

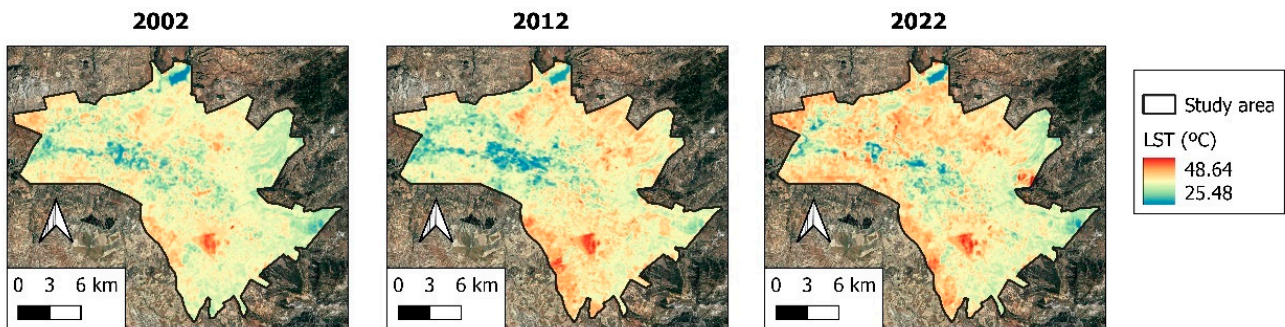


Figure 14. LST between the years 2002 and 2022.

Figure 15 shows the average LST between 2002 and 2022 for each LCZ. It can be seen that the mean temperature was higher in LCZ-10 (37.90 °C), LCZ-2 (37.24 °C), and LCZ-3 (36.84 °C), while the lowest mean LST was found in LCZ-6 (35.32 °C) and LCZ-5 (36.24 °C). In this way, the average LST of urban areas was higher in industrial (37.90%) and compact (37.04 °C) LCZs compared to open areas (35.78%). Figure 16 shows the LST evolution in the different LCZs between the years 2002 and 2022. It can be seen that the largest increases in LST between the years analyzed occurred in the industrial (17.90%) and compact LCZs (13.21%) in contrast to the smaller increases that occurred in the open LCZs (12.50%).

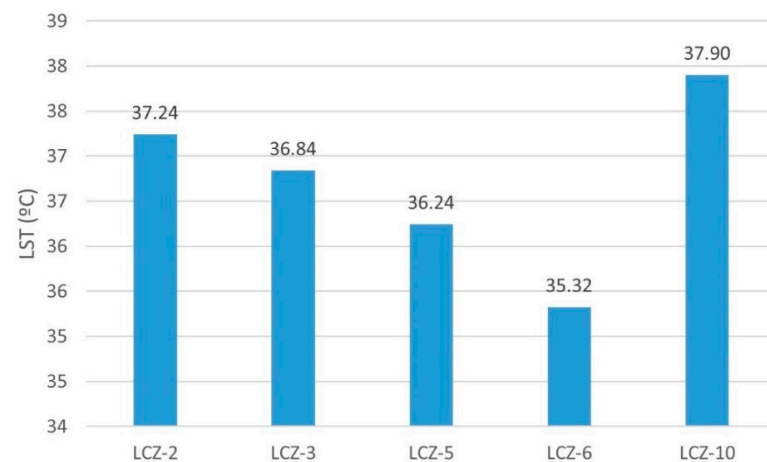


Figure 15. Mean LST for each LCZ of the area under study.

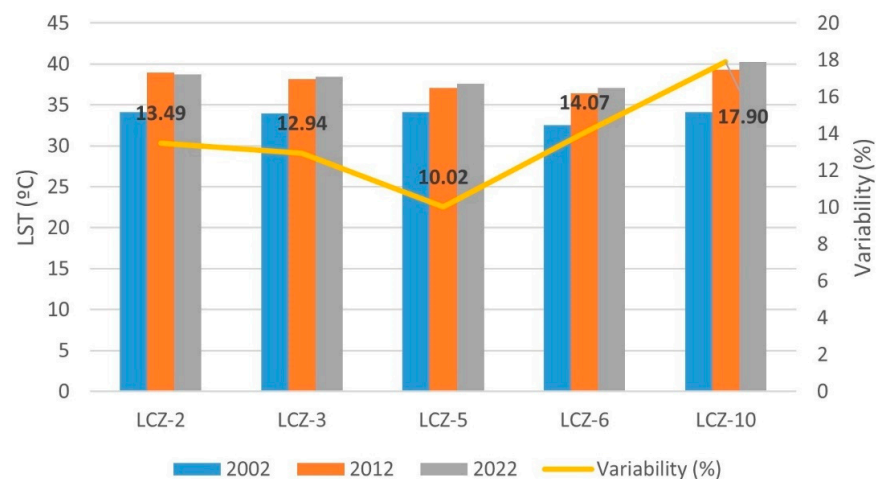


Figure 16. Evolution of LST for years 2002 and 2022 by LCZ.

Applying the Shapiro–Wilk test to the results of the ANOVA test carried out on the temperature indicated that the values did not present normal distributions within the different LCZs since the p value < 0.05 . Therefore, to continue with the ANOVA test for non-normal distributions, it was necessary to perform a Kruskal–Wallis test, the results of which are presented in Table 3.

Table 3. ANOVA test results between the LST and LCZ.

Source	LST
p value	0.005 **
R^2	14.523

Note: errors, ** $p < 0.01$. R^2 : linear regression coefficient.

According to the reported results, the temperature values presented statistically significant relationships of 99% between the different LCZs.

3.5. SUHI

Figure 17 shows the space–time evolution of the SUHI between 2002 and 2022 in the area under study.

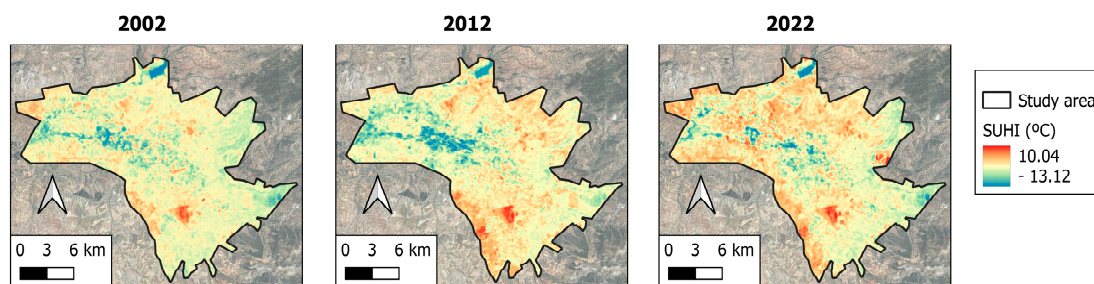


Figure 17. SUHI between the years 2002 and 2022.

The average SUHI in 2002 was 0.21 °C, that of the year 2012 was 0.93 °C, and that of the year 2022 was 1.23 °C. These values represent an average increase of 494.20%. We observed that the highest values of SUHI were concentrated in urban areas and areas without vegetation (higher values for the LST and NDBI index and a lower albedo), while the lowest values were located in rural areas or outside the city (higher values for the NDVI, PV, and albedo indices).

Figure 18 shows the average SUHI between the years 2002 and 2022 for each LCZ. It can be observed that the average SUHI was higher in LCZ-2 (1.36 °C), LCZ-3 (1.28 °C), and LCZ-10 (1.20 °C), while the lowest average SUHI was found in LCZ-6 (0.77 °C) and LCZ-5 (0.78 °C). In this way, the average SUHI of urban areas was higher in industrial (1.20 °C) and compact (1.32 °C) LCZs compared to open areas (0.78%). Figure 19 shows the evolution of SUHI for the different LCZs between 2002 and 2022. It can be seen that the greatest increases in SUHI between the years analyzed occurred in open (235%) and compact (107.13%) LCZs, in contrast to the smaller increases that occurred in industrial LCZs (87.36%).

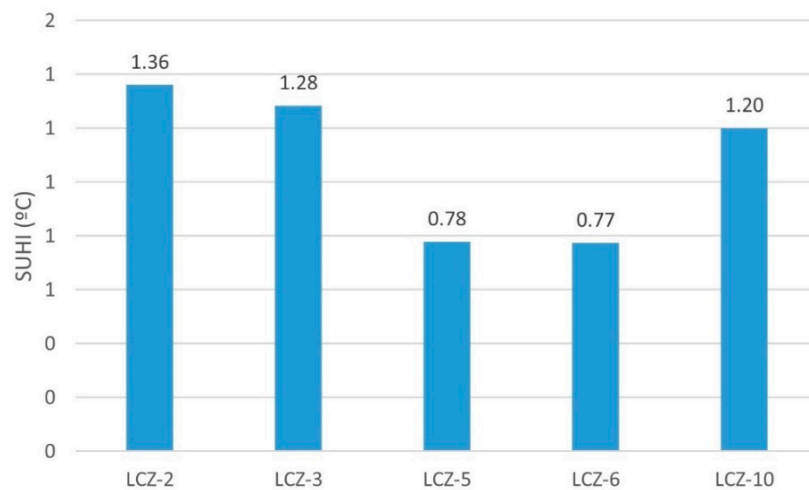


Figure 18. Average SUHI by LCZ.

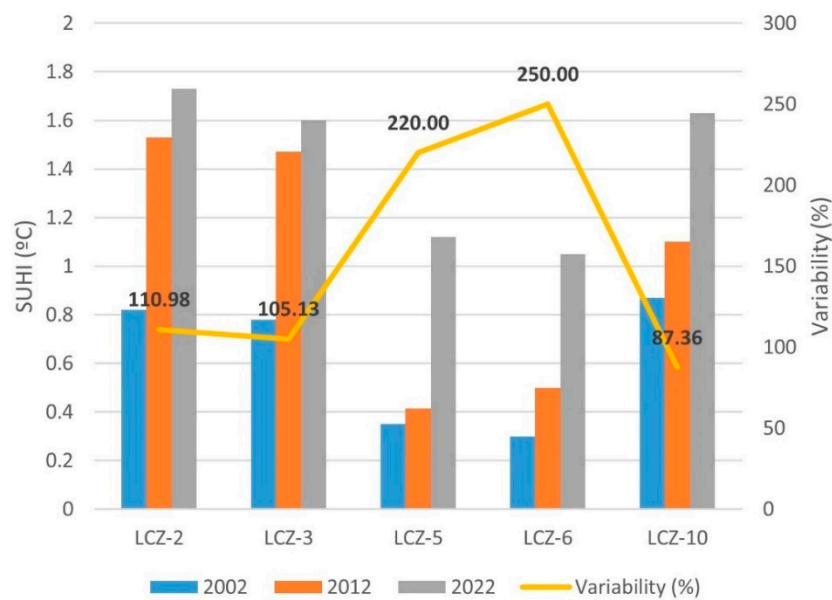


Figure 19. Evolution of the SUHI for each LCZ.

Applying the Shapiro–Wilk test to the results of the ANOVA test carried out on the temperature indicated that the values did not present normal distributions within the different LCZs since the p value < 0.05 . Therefore, to continue with the ANOVA test for non-normal distributions, it was necessary to perform a Kruskal–Wallis test, the results of which can be found in Table 4. According to the reported results, the temperature values presented statistically significant relationships above 99% between the different LCZs.

Table 4. ANOVA test results between the SUHI and LCZ.

Source	SUHI
p value	0.0001 ***
R^2	26.389

Note: errors, *** $p < 0.001$. R^2 : linear regression coefficient.

Next, in order to determine the relationships between SUHI, the NDVI, PV, NDBI, albedo, LULC indices, and the LST and solar radiation variables in the study area, a statistical analysis was carried out using the data panel method. Tables 5 and 6 show the results obtained from this process. Table 5 shows how the SUHI had a positive correlation

with the LST (0.717), NDBI (0.624), albedo (0.455), and LULC (0.385) indices and a negative correlation with the NDVI (−0.588) and PV indices. (−0.627).

Table 5. Pearson’s correlation coefficient between SUHI and indices.

	SUHI	LST	PV	NDVI	NDBI	Radiation	Albedo	LULC
SUHI	1							
LST	0.717	1						
NDVI	−0.588	−0.254	1					
PV	−0.627	−0.151	0.932	1				
NDBI	0.624	0.611	−0.747	−0.655	1			
Radiation	0.099	0.084	0.028	0.031	−0.047	1		
Albedo	0.455	0.078	−0.401	−0.463	0.192	0.099	1	
LULC	0.385	0.327	−0.212	−0.228	0.236	0.162	0.3485	1

Table 6. Data panel results between SUHI and indices.

	β	ρ	sd
LST	0.6768	0.000 ***	0.01178
NDVI	−15.170	0.000 ***	0.44085
PV	−7.7020	0.000 ***	0.55643
NDBI	5.3146	0.000 ***	0.49000
Radiation	0.0007	0.001 **	0.00025
Albedo	12.308	0.000 ***	0.89351
LULC	−0.0614	0.000 ***	0.03841.
Constant	−25.6074	0.000 ***	0.44972
	$R^2 = 0.87$	$F = 1408.19$	$\text{Prob} > \text{chi}^2 = 0.000$

Note: errors, *** $p < 0.001$, ** $p < 0.01$. R^2 : linear regression coefficient; sd: standard deviation; F: statistical variable and β : coefficient.

The data panel technique reported a positive relationship with >99% statistical significance between the variable SUHI and LST, NDBI, albedo, and LULC; a negative relationship with >99% significance between the variables NDVI and PV; and a positive relationship with 95% statistical significance for the radiation variable. We observed a good concordance between the dependent and independent variables by observing the values of R^2 , F, and $\text{Prob} > \text{Chi}^2$. The adjustment level had greater than 99% significance since $\text{Prob} > \text{Chi}^2 = 0.000$. Therefore, the statistical analysis reported the relationships indicated above in an analytical way. Overall, the variables studied in this research presented a statistically significant correlation with the variability of the SUHI. Equation (10) parameterizes these variables and allows us to assess the effectiveness that an increase or reduction in some variables would have:

$$SUHI = 0.6768 \times LST - 7.702 \times NDVI - 15.170 \times PV + 5.314 \times NDBI + 0.0007 \times Radiation + 12.308 \times Albedo - 0.0614 \times LULC - 25.6074. \quad (10)$$

3.6. Effectiveness of Mitigation Measures

Based on the statistical analysis carried out, we applied the following solutions to assess the effectiveness of the mitigation measures selected in the area under study: (1) increasing vegetation by 10%, (2) increasing albedo by 10%, and (3) a combination of proposals 1 and 2.

Our results (Table 7) indicate that the application of proposal 1 in the area under study could yield a 1 °C mitigation of the SUHI, which corresponds to an efficiency of 13.65%, while proposal 2 would produce a 0.93 °C reduction in the SUHI with an efficiency of 12.98%. Finally, a combination of both measures could produce a reduction of 0.82 °C with an efficiency of 12.28%. In this way, the greatest mitigation in terms of temperature and effectiveness would be achieved with proposal 1. However, based on the different

LCZs studied, some variations can be observed in the overall results for the city. Thus, the greatest reduction in SUHI and efficiency percentage of the compact zones (LCZs 2 and 3) was achieved by applying proposal 2, which consisted of increasing the albedo by 10%. Conversely, in open areas (LCZs 5 and 6), the greatest reduction in SUHI and mitigation percentage was achieved with proposal 1, which consisted of increasing green areas by 10%. Lastly, in industrial LCZs, the greatest reduction in SUHI and mitigation percentage was achieved by combining both proposals.

Table 7. Effectiveness of the proposed mitigation measures.

	Proposal 1: 10% Increase Green Area. °C (%)	Proposal 2: Increasing 10% Albedo. °C (%)	Combination of Proposals 1 and 2. °C (%)
Urbe	1.00 (13.65)	0.93 (12.98)	0.82 (12.28)
LCZ-2	0.70 (9.97)	1.32 (14.09)	1.20 (11.40)
LCZ-3	1.08 (12.80)	1.63 (13.39)	1.38 (12.34)
LCZ-5	0.93 (13.33)	0.12 (4.60)	0.75 (10.89)
LCZ-6	1.14 (15.11)	0.28 (5.76)	0.93 (14.47)
LCZ-10	1.10 (13.32)	0.32 (10.65)	1.20 (13.66)

4. Discussion

In general terms, the results obtained indicate that the NDVI, PV, and NDBI indices experienced growth between 2002 and 2022 in the area under study. Conversely, the albedo experienced a decrease in the same period. In turn, within the different LCZs, the NDVI and PV indices related to vegetation presented higher values in open areas (LCZ-5 and LCZ-6) compared to compact urban and industrial areas (LCZ-2, LCZ-3, and LCZ-10), where the values were smaller. In contrast, it was shown that the NDBI index related to buildings had higher compact values (LCZ-2 and LCZ-3) than those in open and industrial areas (LCZ-5, LCZ-6, and LCZ-10), where the values were lower. We found albedo to present higher values in open areas (LCZ-5 and LCZ-6) compared to compact and industrial areas (LCZ-2, LCZ-3 and LCZ-10) where the values were lower.

By definition, compact and industrial areas have higher building densities and building compactness than open areas, which was corroborated by the data obtained in the present study. Thus, the highest values of the NDBI index and the lowest values of the NDVI, PV, and albedo indices were obtained in these areas. Conversely, open LCZs presented lower NDBI values and higher NDVI, PV, and albedo values. From the LULC results, a significant increase in built-up coverage was observed. Additionally, we observed that vegetation coverage was greater in open areas than in compact and industrial areas. These data corroborate those reported on the NDVI and PV indices. These indices determine the urban morphology of each LCZ studied, and the results are in line with similar investigations carried out by other authors [20,64–68] in other cities and territories, granting validity to the results obtained in this research. In this way, the variability detected in the investigated indices was related to the transformation process and changes in land use from rural to urban areas. On the other hand, the variability obtained in the NDVI and PV indices could be assigned not only to the variability of LULC coverage and urban planning systems but also to the variability in rainfall and the drainage system irrigation that may have existed in the area during the period under study [69,70].

There is evidence of a significant increase in LST and SUHI between 2002 and 2022 in the area under study. This increase was greater in industrial and compact areas compared to that in open areas. This result was due to the use of impermeable construction materials with high thermal absorption inside cities, which, after receiving high doses of solar radiation, heat up and subsequently release this heat into the atmosphere [31,68,71]. On the other hand, the LST and SUHI were higher in compact and industrial zones (LCZ-2, LCZ-3, and LCZ-10) than in open zones (LCZ-5 and LCZ-6). This result was also motivated by the configuration of LCZ-5 and LCZ-6 with buildings located at great distances and

large green spaces with vegetation. The former had fewer green areas, lower albedo values, and higher LST and SUHI values. These relationships between temperatures and indices were corroborated by statistical analysis. There are numerous academic studies that corroborate this situation and reveal that an increase in urbanized areas, building density, and impervious soil zones causes an increase in the LST of urban areas [72–77], as well as intensification of SUHI, validating the data obtained in this investigation. Conversely, open areas, which have larger surfaces for vegetation, presented a higher albedo index and lower LST and SUHI values. Numerous studies have shown that vegetation has a cooling effect in urban areas [78–80], ranging between 1 and 3 °C, with warming observed in areas with sparse vegetation and/or bare soil. These phenomena are due not only to the evapotranspiration presented by the vegetation but also to the reflection of solar radiation being greater in these areas than in areas built with impermeable materials [27,30]. Studies carried out in Oregon (USA) reported an average decrease of 1.3 °C in the ambient temperature when the average albedo increased from 0.37 to 0.91 [81]. Numerous studies reported increases in the albedo index with decreases in the LST and SUHI of the studied areas and vice versa [28,29,82] with our results being in line with these previous studies. Studies carried out in the Po River Valley [30] and the city of Termi (Italy) [27] reported SUHI decreases of between 0.5 °C and 2.3 °C, respectively, when the temperature increased, with an albedo between 12 and 3%, in agreement with our results.

Finally, in relation to the effectiveness of the mitigation proposals analyzed, it was reported that both increasing the vegetation surface by 10% and increasing the albedo by 10% have similar rates of effectiveness when it comes to the city in general. A combination of both measures was not found to be appropriate since the results are less effective than those when one of the two proposals is chosen. These results are usually included within the techniques for transforming the urban microclimate by modifying the urban environment by increasing vegetation [25,31]. For example, a study in the city of Mumbai (India) in 2018 reported that an increase in the green areas of the city made it possible to minimize temperatures between 2 and 3 K [33], a study in the city of Singapore between the years 2005 and 2015 reported a cooling effect of the green areas of between 1 and 3 K [34], and a study in the city of Shenzhen (China) between the years 2011 and 2013 reported a temperature decrease of between 0.9 and 1.6 K [83]. However, when the analysis was carried out in the different LCZs, increasing the vegetation surface by 10% in open areas (LCZ-5 and LCZ-6) was more effective than increasing the albedo, while in compact areas, increasing the albedo by 10% was more effective than increasing vegetation. In both areas, it was not appropriate to combine both measures since the effectiveness was less than that achieved by implementing one of the two initial proposals. Finally, in industrial areas, the measure that offered the greatest degree of effectiveness was a combination of the two previous measures. These results may be appropriate if one takes into account that in open areas, vegetation usually predominates over buildings, while in compact and industrial areas, buildings predominate over vegetation. Therefore, if we intervene on the predominant surface type, the success of the mitigation measure will be greater. Numerous studies have analyzed and proposed such mitigation measures in other urban areas [27,32–34,84], achieving results similar to those obtained here. Disaggregated by each LCZ, our results demonstrate that by presenting each area or space with its own morphological, climatic, and urbanization characteristics and maintaining those characteristics over time, the results can be extrapolated to other cities that have the same LCZs. This result was reported by other authors in previous studies that included LCZs as study areas [18,85].

5. Conclusions

This study analyzed the evolution experienced by the SUHI and LST in different LCZs of the Granada metropolitan area between 2002 and 2022 and their relationship with the corresponding indices. After establishing a relationship system, the SUHI mitigation effectiveness of the proposals was evaluated as follows: (1) a 10% increase in green areas, (2) a 10% increase in the albedo index, and (3) a combination of both proposals. These steps

were taken to improve the evaluation capabilities of commonly used mitigation measures, thereby revealing the most appropriate measure and enabling us to extrapolate it to other urban areas.

Our results indicate that between 2002 and 2022, there was an increase in the mean values of LST and SUHI and a decrease in the mean values of albedo. The open LCZs were found to be those that presented the highest values in the NDVI, PV, and albedo indices and, in turn, presented the lowest values of LST and SUHI. Conversely, the compact and industrial zones that presented higher values in the NDBI indices presented lower mean values of albedo and, in turn, higher values of LST and SUHI. These relationships were corroborated by statistical analysis.

In relation to the mitigation measures analyzed, the 10% increase in green areas and albedo and the combination of both measures presented similar efficiencies, granting an approximate decrease in SUHI between 12 and 13%. In the case of closed LCZs, efficiency was improved by decreasing the albedo by 10%, while in open areas, the highest efficiency was achieved by increasing green areas by 10%. Lastly, in industrial areas, the greatest efficiency was achieved by combining both measures: increasing green areas and increasing albedo.

These results show that public administrators and urban planners should, in future developments, prioritize open LZCs with large green spaces, rather than closed LZCs, in order to improve the resilience of cities in the face of future increases in LST and SUHI. On the other hand, in order to improve the quality of life of inhabitants in existing areas, it is necessary to prepare contingency and future urban climate control plans that reward increases in vegetation through the use of roofs and plant facades, as well as the mean increases in albedo in open or compact LCZs. These results could be extrapolated to other cities or urban areas that have the same LZCs as those analyzed here, as such areas would have the same properties.

Funding: This research received no external funding.

Institutional Review Board Statement: Not applicable.

Informed Consent Statement: Not applicable.

Data Availability Statement: Data from this research will be available upon request to the author.

Conflicts of Interest: The author declares no conflict of interest. The funders had no role in the design of the study; in the collection, analyses or interpretation of data; in the writing of the manuscript or in the decision to publish the results.

References

1. An, N.; Dou, J.; González-Cruz, J.E.; Bornstein, R.D.; Miao, S.; Li, L. An observational case study of synergies between an intense heat wave and the urban heat island in Beijing. *J. Appl. Meteorol. Climatol.* **2020**, *59*, 605–620. [[CrossRef](#)]
2. Founda, D.; Santamouris, M. Synergies between Urban Heat Island and Heat Waves in Athens (Greece), during an extremely hot summer (2012). *Sci. Rep.* **2017**, *7*, 10973. [[CrossRef](#)] [[PubMed](#)]
3. Kovats, R.S.; Campbell-Lendrum, D.; Matthies, F. Climate change and human health: Estimating avoidable deaths and disease. *Risk Anal.* **2005**, *25*, 1409–1418. [[CrossRef](#)] [[PubMed](#)]
4. Song, J.; Chen, W.; Zhang, J.; Huang, K.; Hou, B.; Prishchepov, A.V. Effects of building density on land surface temperature in China: Spatial patterns and determinants. *Landsc. Urban Plan.* **2020**, *198*, 103794. [[CrossRef](#)]
5. Meehl, G.A.; Tebaldi, C. More intense, more frequent, and longer lasting heat waves in the 21st century. *Science* **2004**, *305*, 994–997. [[CrossRef](#)]
6. Sun, Y.; Zhang, X.; Zwiers, F.W.; Song, L.; Wan, H.; Hu, T.; Yin, H.; Ren, G. Rapid increase in the risk of extreme summer heat in Eastern China. *Nat. Clim. Change* **2014**, *4*, 1082–1085. [[CrossRef](#)]
7. Coumou, D.; Robinson, A.; Rahmstorf, S. Global increase in record-breaking monthly-mean temperatures. *Clim. Change* **2013**, *118*, 771–782. [[CrossRef](#)]
8. Lau, N.C.; Nath, M.J. A model study of heat waves over North America: Meteorological aspects and projections for the twenty-first century. *J. Clim.* **2012**, *25*, 4761–4764. [[CrossRef](#)]
9. IPCC. *The Fifth Report of the Intergovernmental Panel on Climate Change (IPCC)*; IPCC: Geneva, Switzerland, 2013. Available online: <https://www.ipcc.ch/report/ar5/wg1/> (accessed on 23 April 2023).

10. UNO. *68% of the World Population Projected to Live in Urban Areas by 2050, Says UN*; UNO: New York, NY, USA, 2018. Available online: <https://www.un.org/development/desa/en/news/population/2018-revision-of-world-urbanization-prospects.html> (accessed on 23 April 2023).
11. Mukherjee, S.; Debnath, A. Correlation between Land Surface Temperature and Urban Heat Island with COVID-19 in New Delhi, India. *Res. Sq.* **2020**, 1–11.
12. Schneider, A.; Friedl, M.A.; Potere, D. Mapping global urban areas using MODIS 500-m data: New methods and datasets based on “urban ecoregions”. *Remote Sens. Environ.* **2010**, *114*, 1733–1746. [[CrossRef](#)]
13. Li, J.; Song, C.; Cao, L.; Zhu, F.; Meng, X.; Wu, J. Impacts of landscape structure on surface urban heat islands: A case study of Shanghai, China. *Remote Sens. Environ.* **2011**, *115*, 3249–3263. [[CrossRef](#)]
14. Stewart, I.D.; Oke, T.R. Local climate zones for urban temperature studies. *Bull. Am. Meteorol. Soc.* **2012**, *93*, 1879–1900. [[CrossRef](#)]
15. Arnfield, A.J. Two decades of urban climate research: A review of turbulence, exchanges of energy and water, and the urban heat island. *Int. J. Climatol.* **2003**, *23*, 1–26. [[CrossRef](#)]
16. Zhou, D.; Zhao, S.; Zhang, L.; Sun, G.; Liu, Y. The footprint of urban heat island effect in China. *Sci. Rep.* **2015**, *5*, 2–12. [[CrossRef](#)]
17. Santamouris, M. Recent progress on urban overheating and heat island research. Integrated assessment of the energy, environmental, vulnerability and health impact. Synergies with the global climate change. *Energy Build.* **2020**, *207*, 109482.
18. Das, M.; Das, A. Assessing the relationship between local climatic zones (LCZs) and land surface temperature (LST)—A case study of Sriniketan-Santiniketan Planning Area (SSPA), West Bengal, India. *Urban Clim.* **2020**, *32*, 100591. [[CrossRef](#)]
19. Guo, A.; Yang, J.; Xiao, X.; Xia (Cecilia), J.; Jin, C.; Li, X. Influences of urban spatial form on urban heat island effects at the community level in China. *Sustain. Cities Soc.* **2020**, *53*, 101972. [[CrossRef](#)]
20. Hidalgo García, D.; Arco Díaz, J. Modeling of the Urban Heat Island on local climatic zones of a city using Sentinel 3 images: Urban determining factors. *Urban Clim.* **2021**, *37*, 100840. [[CrossRef](#)]
21. Hua, L.; Zhang, X.; Nie, Q.; Sun, F.; Tang, L. The impacts of the expansion of urban impervious surfaces on urban heat islands in a coastal city in China. *Sustainability* **2020**, *12*, 475. [[CrossRef](#)]
22. Khamchiangta, D.; Dhakal, S. Physical and non-physical factors driving urban heat island: Case of Bangkok Metropolitan Administration, Thailand. *J. Environ. Manag.* **2019**, *248*, 109285. [[CrossRef](#)]
23. Mora, C.; Dousset, B.; Caldwell, I.R.; Powell, F.E.; Geronimo, R.C.; Bielecki, C.R.; Counsell, C.W.; Dietrich, B.S.; Johnston, E.T.; Louis, L.V.; et al. Global risk of deadly heat. *Nat. Clim. Change* **2017**, *7*, 501–506. [[CrossRef](#)]
24. Marcotullio, P.J.; Keßler, C.; Fekete, B.M. Global urban exposure projections to extreme heatwaves. *Front. Built Environ.* **2022**, *8*, 947496. [[CrossRef](#)]
25. Solecki, W.D.; Rosenzweig, C.; Parshall, L.; Pope, G.; Clark, M.; Cox, J.; Wiencke, M. Mitigation of the heat island effect in urban New Jersey. *Environ. Hazards* **2005**, *6*, 39–49. [[CrossRef](#)]
26. Tewari, M.; Yang, J.; Kusaka, H.; Salamanca, F.; Watson, C.; Treinish, L. Interaction of urban heat islands and heat waves under current and future climate conditions and their mitigation using green and cool roofs in New York City and Phoenix, Arizona. *Environ. Res. Lett.* **2019**, *14*, 034002. [[CrossRef](#)]
27. Bonafoni, S.; Baldinelli, G.; Verducci, P. Sustainable strategies for smart cities: Analysis of the town development effect on surface urban heat island through remote sensing methodologies. *Sustain. Cities Soc.* **2017**, *29*, 211–218. [[CrossRef](#)]
28. Karbalaee, A.R.; Hedjazizadeh, Z.; Masoodian, S.A.; Keikhosravi-Kiany, M.S. Investigating the land surface albedo trend in Iran using remote sensing data. *Theor. Appl. Climatol.* **2022**, *150*, 389–403. [[CrossRef](#)]
29. Hamoodi, M.N.; Corner, R.; Dewan, A. Thermophysical behaviour of LULC surfaces and their effect on the urban thermal environment. *J. Spat. Sci.* **2019**, *64*, 111–130. [[CrossRef](#)]
30. Costanzini, S.; Despini, F.; Beltrami, L.; Fabbi, S.; Muscio, A.; Teggi, S. Identification of SUHI in Urban Areas by Remote Sensing Data and Mitigation Hypothesis through Solar Reflective Materials. *Atmosphere* **2022**, *13*, 70. [[CrossRef](#)]
31. Saaroni, H.; Amorim, J.H.; Hiemstra, J.A.; Pearlmutter, D. Urban Green Infrastructure as a tool for urban heat mitigation: Survey of research methodologies and findings across different climatic regions. *Urban Clim.* **2018**, *24*, 94–110. [[CrossRef](#)]
32. Gago, E.J.; Roldan, J.; Pacheco-Torres, R.; Ordóñez, J. The city and urban heat islands: A review of strategies to mitigate adverse effects. *Renew. Sustain. Energy Rev.* **2013**, *25*, 749–758. [[CrossRef](#)]
33. Dwivedi, A.; Mohan, B.K. Impact of green roof on micro climate to reduce Urban Heat Island. *Remote Sens. Appl. Soc. Environ.* **2018**, *10*, 56–69. [[CrossRef](#)]
34. Masoudi, M.; Tan, P.Y.; Fadaei, M. The effects of land use on spatial pattern of urban green spaces and their cooling ability. *Urban Clim.* **2021**, *35*, 100743. [[CrossRef](#)]
35. Song, J.; Lin, T.; Li, X.; Prishchepov, A.V. Mapping urban functional zones by integrating very high spatial resolution remote sensing imagery and points of interest: A case study of Xiamen, China. *Remote Sens.* **2018**, *10*, 1737. [[CrossRef](#)]
36. Tepanosyan, G.; Muradyan, V.; Hovsepyan, A.; Pinigin, G.; Medvedev, A.; Asmaryan, S. Studying spatial-temporal changes and relationship of land cover and surface Urban Heat Island derived through remote sensing in Yerevan, Armenia. *Build. Environ.* **2021**, *187*, 107390. [[CrossRef](#)]
37. Ngarambe, J.; Nganyiyimana, J.; Kim, I.; Santamouris, M.; Young Yun, G. Synergies between urban heat island and heat waves in Seoul: The role of wind speed and land use characteristics. *PLoS ONE* **2020**, *15*, e0243571. [[CrossRef](#)]
38. Wang, J.; Ouyang, W. Attenuating the surface Urban Heat Island within the Local Thermal Zones through land surface modification. *J. Environ. Manag.* **2017**, *187*, 239–252. [[CrossRef](#)]

39. Stewart, I.; Oke, T. Classifying Urban Climate Field Sites by “Local Climate Zones”: The Case of Nagano, Japan. In Proceedings of the Seventh International Conference on Urban Climate, Yokohama, Japan, 29 June–3 July 2009; pp. 1–5.
40. Cramer, W.; Guiot, J.; Fader, M.; Garrabou, J.; Gattuso, J.P.; Iglesias, A.; Lange, M.A.; Lionello, P.; Llasat, M.C.; Paz, S.; et al. Climate change and interconnected risks to sustainable development in the Mediterranean. *Nat. Clim. Change* **2018**, *8*, 972–980. [[CrossRef](#)]
41. Ward, K.; Lauf, S.; Kleinschmit, B.; Endlicher, W. Heat waves and urban heat islands in Europe: A review of relevant drivers. *Sci. Total Environ.* **2016**, *569–570*, 527–539. [[CrossRef](#)]
42. De Castro, M.; Gallardo, C.; Jylha, K.; Tuomenvirta, H. The use of a climate-type classification for assessing climate change effects in Europe from an ensemble of nine regional climate models. *Clim. Change* **2007**, *81*, 329–341. [[CrossRef](#)]
43. Amindin, A.; Pouyan, S.; Pourghasemi, H.R.; Yousefi, S.; Tiefenbacher, J.P. Spatial and temporal analysis of urban heat island using Landsat satellite images. *Environ. Sci. Pollut. Res.* **2021**, *28*, 41439–41450. [[CrossRef](#)]
44. Shafizadeh-Moghadam, H.; Weng, Q.; Liu, H.; Valavi, R. Modeling the spatial variation of urban land surface temperature in relation to environmental and anthropogenic factors: A case study of Tehran, Iran. *GIScience Remote Sens.* **2020**, *57*, 483–496. [[CrossRef](#)]
45. Campbell, J. *Introduction to Remote Sensing*, 2nd ed.; Guilford Press: London, UK, 1996.
46. Anjos, M.; Targino, A.C.; Krecl, P.; Oukawa, G.Y.; Braga, R.F. Analysis of the urban heat island under different synoptic patterns using local climate zones. *Build. Environ.* **2020**, *185*, 107268. [[CrossRef](#)]
47. Brousse, O.; Georganos, S.; Demuzere, M.; Vanhuyse, S.; Wouters, H.; Wolff, E.; Linard, C.; Nicole, P.M.; Dujardin, S. Using Local Climate Zones in Sub-Saharan Africa to tackle urban health issues. *Urban Clim.* **2019**, *27*, 227–242. [[CrossRef](#)]
48. Emmanuel, R.; Krüger, E. Urban heat island and its impact on climate change resilience in a shrinking city: The case of Glasgow, UK. *Build. Environ.* **2012**, *53*, 137–149. [[CrossRef](#)]
49. Equere, V.; Mirzaei, P.A.; Riffat, S. Definition of a new morphological parameter to improve prediction of urban heat island. *Sustain. Cities Soc.* **2020**, *56*, 102021. [[CrossRef](#)]
50. Zhang, Y.; Chen, L.; Wang, Y.; Chen, L.; Yao, F.; Wu, P.; Li, Y.; Zhou, T.; Zhang, T. Research on the contribution of urban land surface moisture to the alleviation effect of urban land surface heat based on landsat 8 data. *Remote Sens.* **2015**, *7*, 10737–10762. [[CrossRef](#)]
51. Congedo, L. Semi-Automatic Classification Plugin Documentation Release 4.8.0.1. *Release* **2016**, *4*, 29. Available online: <https://media.readthedocs.org/pdf/semiautomaticclassificationmanual-v4/latest/semiautomaticclassificationmanual-v4.pdf> (accessed on 23 April 2023).
52. Logan, T.M.; Zaitchik, B.; Guikema, S.; Nisbet, A. Night and day: The influence and relative importance of urban characteristics on remotely sensed land surface temperature. *Remote Sens. Environ.* **2020**, *247*, 111861. [[CrossRef](#)]
53. Yu, X.; Guo, X.; Wu, Z. Land surface temperature retrieval from landsat 8 TIRS-comparison between radiative transfer equation-based method, split window algorithm and single channel method. *Remote Sens.* **2014**, *6*, 9829–9852. [[CrossRef](#)]
54. García, D.H.; Díaz, J.A. Space–time analysis of the earth’s surface temperature, surface urban heat island and urban hotspot: Relationships with variation of the thermal field in Andalusia (Spain). *Urban Ecosyst.* **2023**, *26*, 525–546. [[CrossRef](#)]
55. Zha, Y.; Gao, J.; Ni, S. Use of normalized difference built-up index in automatically mapping urban areas from TM imagery. *Int. J. Remote Sens.* **2003**, *24*, 583–594. [[CrossRef](#)]
56. Liang, S.; Shuey, C.J.; Russ, A.L.; Fang, H.; Chen, M.; Walthall, C.L.; Daughtry, C.S.; Hunt, R., Jr. Narrowband to broadband conversions of land surface albedo: II. Validation. *Remote Sens. Environ.* **2003**, *84*, 25–41. [[CrossRef](#)]
57. Kafer, P.S.; Rolim, S.B.A.; Iglesias, M.L.; Da Rocha, N.S.; Diaz, L.R. Land surface temperature retrieval by landsat 8 thermal band: Applications of laboratory and field measurements. *IEEE J. Sel. Top. Appl. Earth Obs. Remote Sens.* **2019**, *12*, 2332–2341. [[CrossRef](#)]
58. Sharma, R.; Pradhan, L.; Kumari, M.; Bhattacharya, P. Assessing urban heat islands and thermal comfort in Noida City using geospatial technology. *Urban Clim.* **2021**, *35*, 100751. [[CrossRef](#)]
59. Weng, Q.; Lu, D.; Schubring, J. Estimation of land surface temperature-vegetation abundance relationship for urban heat island studies. *Remote Sens. Environ.* **2004**, *89*, 467–483. [[CrossRef](#)]
60. Oke, T.R. *Boundary Layer Climates*; Routledge: London, UK, 1987.
61. Conrad, O.; Bechtel, B.; Bock, M.; Dietrich, H.; Fischer, E.; Gerlitz, L.; Wehberg, J.; Wichmann, V.; Böhner, J. System for Automated Geoscientific Analyses (SAGA) v. 2.1.4. *Geosci. Model Dev. Discuss.* **2015**, *8*, 2271–2312. [[CrossRef](#)]
62. Bremer, M.; Mayr, A.; Wichmann, V.; Schmidtner, K.; Rutzinger, M. A new multi-scale 3D-GIS-approach for the assessment and dissemination of solar income of digital city models. *Comput. Environ. Urban Syst.* **2016**, *57*, 144–154. [[CrossRef](#)]
63. Zakšek, K.; Podobnikar, T.; Oštir, K. Solar radiation modelling. *Comput. Geosci.* **2005**, *31*, 233–240. [[CrossRef](#)]
64. Avdan, U.; Jovanovska, G. Algorithm for automated mapping of land surface temperature using LANDSAT 8 satellite data. *J. Sens.* **2016**, *2016*, 1480307. [[CrossRef](#)]
65. Diallo-Dudek, J.; Lacaze, B.; Comby, J. Land surface temperature in the urban area of Lyon metropolis: A comparative study of remote sensing data and MesoNH model simulation. In Proceedings of the 2015 Joint Urban Remote Sensing Event (JURSE), Lausanne, Switzerland, 30 March–1 April 2015; IEEE: Piscataway, NJ, USA, 2015; Volume 2015, pp. 2–5.
66. Kafy, A.A.; Rahman, M.S.; Islam, M.; Al Rakib, A.; Islam, M.A.; Khan, M.H.H.; Sikdar, M.S.; Sarker, M.H.S.; Mawa, J.; Sattar, G.S. Prediction of seasonal urban thermal field variance index using machine learning algorithms in Cumilla, Bangladesh. *Sustain. Cities Soc.* **2021**, *64*, 102542. [[CrossRef](#)]

67. Wang, T.; Shi, J.; Ma, Y.; Husi, L.; Comyn-Platt, E.; Ji, D.; Zhao, T.; Xiong, C. Recovering Land Surface Temperature Under Cloudy Skies Considering the Solar-Cloud-Satellite Geometry: Application to MODIS and Landsat-8 Data. *J. Geophys. Res. Atmos.* **2019**, *124*, 3401–3416. [[CrossRef](#)]
68. Yang, C.; Yan, F.; Zhang, S. Comparison of land surface and air temperatures for quantifying summer and winter urban heat island in a snow climate city. *J. Environ. Manag.* **2020**, *265*, 110563. [[CrossRef](#)] [[PubMed](#)]
69. Li, B.; Tao, S.; Dawson, R.W. Relations between AVHRR NDVI and ecoclimatic parameters in China. *Int. J. Remote Sens.* **2002**, *23*, 989–999. [[CrossRef](#)]
70. Nicholson, S.E.; Farrar, T.J. The influence of soil type on the relationships between NDVI, rainfall, and soil moisture in semiarid Botswana. I. NDVI response rainfall. *Remote Sens. Environ.* **1994**, *50*, 107–120. [[CrossRef](#)]
71. Wu, C.; Li, J.; Wang, C.; Song, C.; Chen, Y.; Finka, M.; La Rosa, D. Understanding the relationship between urban blue infrastructure and land surface temperature. *Sci. Total Environ.* **2019**, *694*, 133742. [[CrossRef](#)] [[PubMed](#)]
72. Feizizadeh, B.; Blaschke, T. Examining Urban heat Island relations to land use and air pollution: Multiple endmember spectral mixture analysis for thermal remote sensing. *IEEE J. Sel. Top. Appl. Earth Obs. Remote Sens.* **2013**, *6*, 1749–1756. [[CrossRef](#)]
73. Keramitsoglou, I.; Kiranoudis, C.T.; Ceriola, G.; Weng, Q.; Rajasekar, U. Identification and analysis of urban surface temperature patterns in Greater Athens, Greece, using MODIS imagery. *Remote Sens. Environ.* **2011**, *115*, 3080–3090. [[CrossRef](#)]
74. Lemus-Canovas, M.; Martin-Vide, J.; Moreno-Garcia, M.C.; Lopez-Bustins, J.A. Estimating Barcelona’s metropolitan daytime hot and cold poles using Landsat-8 Land Surface Temperature. *Sci. Total Environ.* **2020**, *699*, 134307. [[CrossRef](#)]
75. Li, T.; Meng, Q. A mixture emissivity analysis method for urban land surface temperature retrieval from Landsat 8 data. *Landsc. Urban Plan.* **2018**, *179*, 63–71. [[CrossRef](#)]
76. Mallick, J.; Rahman, A.; Singh, C.K. Modeling urban heat islands in heterogeneous land surface and its correlation with impervious surface area by using night-time ASTER satellite data in highly urbanizing city, Delhi-India. *Adv. Space Res.* **2013**, *52*, 639–655. [[CrossRef](#)]
77. Tsou, J.; Zhuang, J.; Li, Y.; Zhang, Y. Urban Heat Island Assessment Using the Landsat 8 Data: A Case Study in Shenzhen and Hong Kong. *Urban Sci.* **2017**, *1*, 10. [[CrossRef](#)]
78. Du, J.; Xiang, X.; Zhao, B.; Zhou, H. Impact of urban expansion on land surface temperature in Fuzhou, China using Landsat imagery. *Sustain. Cities Soc.* **2020**, *61*, 102346. [[CrossRef](#)]
79. Lin, W.; Yu, T.; Chang, X.; Wu, W.; Zhang, Y. Calculating cooling extents of green parks using remote sensing: Method and test. *Landsc. Urban Plan.* **2015**, *134*, 66–75. [[CrossRef](#)]
80. Qiu, G.Y.; Zou, Z.; Li, X.; Li, H.; Guo, Q.; Yan, C.; Tan, S. Experimental studies on the effects of green space and evapotranspiration on urban heat island in a subtropical megacity in China. *Habitat Int.* **2017**, *68*, 30–42. [[CrossRef](#)]
81. Taleghani, M.; Sailor, D.J.; Tenpierik, M.; van den Dobbelsteen, A. Thermal assessment of heat mitigation strategies: The case of Portland State University, Oregon, USA. *Build. Environ.* **2014**, *73*, 138–150. [[CrossRef](#)]
82. Menon, S.; Akbari, H.; Mahanama, S.; Sednev, I.; Levinson, R. Radiative forcing and temperature response to changes in urban albedos and associated CO₂ offsets. *Environ. Res. Lett.* **2010**, *5*, 014005. [[CrossRef](#)]
83. Majumder, A.; Setia, R.; Kingra, P.K.; Sembhi, H.; Singh, S.P.; Pateriya, B. Estimation of land surface temperature using different retrieval methods for studying the spatiotemporal variations of surface urban heat and cold islands in Indian Punjab. *Environ. Dev. Sustain.* **2021**, *23*, 15921–15942. [[CrossRef](#)]
84. Deilami, K.; Kamruzzaman, M.; Liu, Y. Urban heat island effect: A systematic review of spatio-temporal factors, data, methods, and mitigation measures. *Int. J. Appl. Earth Obs. Geoinf.* **2018**, *67*, 30–42. [[CrossRef](#)]
85. Kotharkar, R.; Ghosh, A.; Kotharkar, V. Estimating summertime heat stress in a tropical Indian city using Local Climate Zone (LCZ) framework. *Urban Clim.* **2021**, *36*, 100784. [[CrossRef](#)]

Disclaimer/Publisher’s Note: The statements, opinions and data contained in all publications are solely those of the individual author(s) and contributor(s) and not of MDPI and/or the editor(s). MDPI and/or the editor(s) disclaim responsibility for any injury to people or property resulting from any ideas, methods, instructions or products referred to in the content.